

# Lawrence Berkeley National Laboratory

## Recent Work

### Title

Tunable charge to spin conversion in strontium iridate thin films

### Permalink

<https://escholarship.org/uc/item/4847601j>

### Journal

Physical Review Materials, 3(5)

### ISSN

2475-9953

### Authors

Everhardt, AS  
Dc, M  
Huang, X  
[et al.](#)

### Publication Date

2019-05-06

### DOI

10.1103/PhysRevMaterials.3.051201

Peer reviewed

# 1 Tunable charge to spin conversion in strontium iridate thin films

2 Arnoud S. Everhardt\*<sup>1,2‡</sup>, Mahendra DC\*<sup>3</sup>, Xiaoxi Huang<sup>2</sup>, Shehrin Sayed<sup>4,5</sup>, Tanay Gosavi<sup>6</sup>, Yunlong  
3 Tang<sup>1,2</sup>, Chia-Ching Lin<sup>6</sup>, Sasikanth Manipatruni<sup>6</sup>, Ian Young<sup>6</sup>, Supriyo Datta<sup>5</sup>, Jian-Ping Wang<sup>3</sup>,  
4 Ramamoorthy Ramesh<sup>1,2‡</sup>

5 <sup>1</sup> Materials Sciences Division, Lawrence Berkeley National Laboratory, Berkeley, CA 94720, USA

6 <sup>2</sup> Department of Materials Science and Engineering and Department of Physics, University of California, Berkeley,  
7 CA 94720

8 <sup>3</sup> School of Physics and Astronomy, University of Minnesota, Minneapolis, MN, USA

9 <sup>4</sup> Department of Electrical Engineering and Computer Science, University of California, Berkeley, CA 94720

10 <sup>5</sup> School of Electrical and Computer Engineering, Purdue University, West Lafayette, Indiana 47907, USA

11 <sup>6</sup> Intel Corporation

12 \* These authors contributed equally

13 ‡ Corresponding authors: [arnoudeverhardt@lbl.gov](mailto:arnoudeverhardt@lbl.gov); [rramesh@berkeley.edu](mailto:rramesh@berkeley.edu)

14 **Abstract:** Efficient charge to spin conversion is important for low power spin logic devices. Spin and  
15 charge interconversion is commonly performed using heavy metals and topological insulators, while the  
16 field of oxides is not yet fully explored. Strontium iridate thin films were grown, where the different  
17 crystal structures form a perfect playground to understand the key factors in obtaining high charge to  
18 spin conversion efficiency (i.e., large spin Hall angle). It was found that the semiconducting Sr<sub>2</sub>IrO<sub>4</sub> has a  
19 spin Hall angle of ~0.1 (depending on measurement technique), which is promising for a spin-orbit  
20 coupled electronic system and comparable to Pt. In contrast, the perovskite SrIrO<sub>3</sub>, reported to have a  
21 Dirac cone near the Fermi level, has a larger spin Hall angle of 0.3-0.4 degrees. The largest difference  
22 between the two materials is a large degree of spin-momentum locking in SrIrO<sub>3</sub>, comparable to known  
23 topological insulators. A simple semi-classical relationship is found where the spin Hall angle increases  
24 for higher degrees of spin-momentum locking and it also increases for lower Fermi wave vectors. This  
25 relationship is then able to explain the decreased spin Hall angle below 10 nm film thickness in SrIrO<sub>3</sub>, by  
26 relating it to the correspondingly higher carrier concentration (related to the higher Fermi wave vector).  
27 Breaking the commonly believed anti-correlation between resistivity and carrier concentration paves a  
28 pathway to lower power losses due to resistance while keeping large spin Hall angles.

## 1 **Main text**

2 Transition metal oxides provide a rich playground for a variety of fundamental physical phenomena that  
3 have led to discoveries such as high temperature superconductivity in cuprates, colossal  
4 magnetoresistance in doped manganites[1], and multiferroic behavior[2]. Many oxide materials are  
5 used for their versatile properties and high adaptability, ranging from metallic to insulating[3],  
6 magnetic[4,5] and, in the case of 4d and 5d transition metal oxides, large spin-orbit coupling[6]. Small  
7 variations in elemental composition[7,8], boundary conditions, interface effects[9] or strain[10] in thin  
8 films can have a profound influence on such physical phenomena. One of the scientific challenges in the  
9 field of spintronics these days is the manipulation and interconversion of spin and charge. Spintronic  
10 logic devices, such as a spin-orbit torque magnetoresistive random access memory (SOT-MRAM)[11,12],  
11 skyrmionic[13] or magnetoelectric spin orbit logic[14–16] require a low-power highly efficient  
12 interconversion of spin to charge, which is given as the spin Hall angle. There have been several studies  
13 of the (inverse) spin Hall and Rashba-Edelstein effects in heavy metals[17,18] and  
14 semiconductors[19,20]. Recently, extensions into topological insulators that exhibit large spin orbit  
15 coupling[21–25] and 2D electron gas systems[9] have revealed a larger degree of interconversion. The  
16 generally observed trend is that, for sufficiently heavy elements, increasing the resistivity leads to an  
17 enhancement of the spin and charge intercoupling[26,27], most notably in the series of increasing  
18 coupling for the heavy metals Au[28], Pt[29], Ta[18] and W[30]. A merging of spintronics with the wide  
19 tunability in electronic properties provided by oxide materials will be able to provide novel pathways  
20 towards high charge and spin coupling with lower power requirements.

21 Oxides, especially the ones in which one or more of the chemical sublattices is comprised of high spin-  
22 orbit coupled chemical species (e.g.,  $\text{Ir}^{4+}$  in iridates) present an interesting opportunity to explore the  
23 role of strong spin-orbit coupling, tunability of electronic structure, resistivity and carrier concentrations  
24 as well as the potential to introduce correlations as an active parameter[6]. The physics in the material  
25 class of iridates[6,31–33] is driven by the electronic structure of the  $\text{Ir}^{4+}$  ion. As a direct consequence of  
26 the large atomic number, spin-orbit coupling is much stronger than the commonly used 3d elements.  
27 The competition between the increased spin-orbit coupling and the decreased electron correlation  
28 strength,  $U$ , due to larger orbital extension provides a rich physics playground with phenomena like  
29 topological Mott insulators, spin liquids and Weyl semimetals[6]. Several crystal classes manifest  
30 themselves within the family of iridates, particularly in the Ruddlesden-Popper series of  $\text{Sr}_{n+1}\text{Ir}_n\text{O}_{3n+1}$  with  
31 its endmembers  $\text{SrIrO}_3$  and  $\text{Sr}_2\text{IrO}_4$ , and in the pyrochlores with the stoichiometry  $\text{A}_2\text{Ir}_2\text{O}_7$ . Within each

1 family, an extensive range of chemical substitutions is available to systematically tune the electronic  
2 interactions.

3 The layered perovskite  $\text{Sr}_2\text{IrO}_4$  manages to overcome the expected metallic state by forming several  
4 narrow bands due to strong spin-orbit interaction. Then a small, but non-zero electronic repulsion  
5 energy  $U$  (responsible for Mott insulating states) is enough to split those narrow bands to make this  
6 material weakly semiconducting with a bandgap of  $\sim 0.5$  eV[34]. In contrast, the perovskite  $\text{SrIrO}_3$  has an  
7 intrinsic metallic state by overcoming those band splittings due to increased dimensionality and  
8 decreased octahedral rotations[35]. However, going towards large compressive strain [31] or to lower  
9 ( $< 5$  nm) thicknesses [32], it manifests a metal-insulator transition. Furthermore, a highly interesting  
10 behavior in  $\text{SrIrO}_3$ , not found in  $\text{Sr}_2\text{IrO}_4$ , is its semimetallic state with a Dirac cone crossing the Fermi  
11 level, predicted theoretically[36] and found in ARPES measurements[35,37]. This indicates that the  
12 material should have a high degree of spin-momentum locking like in topological insulators and thus a  
13 large charge to spin interconversion[38].

14 High-quality strontium iridate thin films were grown from stoichiometric targets by Pulsed Laser  
15 Deposition of  $\text{SrIrO}_3$  ( $\text{Sr}_2\text{IrO}_4$ ) on an LSAT substrate[39–41] using temperature  $T = 700$  °C (850 °C), oxygen  
16 pressure  $P_{\text{O}_2} = 0.13$  mbar (0.004 mbar), laser repetition rate = 2 Hz (1 Hz) and laser fluence =  $1.5$  J/cm<sup>2</sup> ( $2$   
17 J/cm<sup>2</sup>). Ferromagnetic NiFe (permalloy,  $\text{Ni}_{0.79}\text{Fe}_{0.19}$ ) as spin detection layer and oxide capping layers ( $\text{AlO}_x$   
18 or MgO) were sputtered *ex-situ*. Fig. 1 shows the structure of the films with the perovskite  $\text{SrIrO}_3$  and  
19 the layered structure  $\text{Sr}_2\text{IrO}_4$ .  $\text{SrIrO}_3$  is on the border between metallic and insulating as expected for this  
20 strain state[39], with a minimum in the resistivity at 200 K, increased carrier concentration and  
21 decreased mobility for higher temperatures for the 10 nm thick  $\text{SrIrO}_3$ , while 5 nm  $\text{SrIrO}_3$  has decreasing  
22 resistivity for higher temperatures combined with flat mobility and increased carrier concentration as an  
23 insulating state. So the metal-insulator transition takes place between 10 and 5 nm, higher than  
24 reported on low-strain substrates[32] due to the increased compressive strain[31] aiding in the metal-  
25 insulator transition.  $\text{Sr}_2\text{IrO}_4$  is semiconducting over all thicknesses with  $> 1000x$  higher resistivity than  
26  $\text{SrIrO}_3$ . The 5 nm  $\text{Sr}_2\text{IrO}_4$  was too resistive to measure its resistivity and the Hall coefficients could not be  
27 determined with more accuracy than a lower bound of  $10^{20}$ - $10^{21}$  cm<sup>-3</sup>, comparable to that of metallic  
28  $\text{SrIrO}_3$ .

29 The characterization of the charge to spin conversion was performed by looking at the effect an injected  
30 charge current in the grown spin Hall material/ferromagnet bilayer (iridate/NiFe in this study) has on the  
31 magnetization of the ferromagnet. Following an injected charge current flowing laterally along the x-

1 axis, the spin Hall effect generates spin currents perpendicular (along the z-axis) to the applied charge  
2 current in the iridate material as sketched in Fig 2a, while the Rashba-Edelstein effect generates non-  
3 equilibrium spin accumulation near the iridate/NiFe interface which can diffuse into the ferromagnet,  
4 also perpendicular (along the z-axis) to the charge current. Those spin currents exert a torque on the  
5 magnetization in the ferromagnetic material NiFe. The first torque exerted is the anti-damping-like  
6 torque, a torque parallel (along the y-axis) to the surface  $\tau_{DL}$  or  $\tau_{||}$ , which produces an effective out-of-  
7 plane field  $H_{OOP}$ [42,43]. The second torque observed in these measurement configurations are the  
8 Oersted torques  $\tau_{Oe}$ , which exert the torque perpendicular to the surface (along the z-axis) and they are  
9 generated by the charge current flow in the non-magnetic layer due to Ampère's law. Knowing these  
10 two torques, it becomes possible to calculate the spin Hall angle by measuring the ratio of these two  
11 torques, as both  $\tau_{DL}$  and the Oersted field  $\tau_{Oe}$  depend only on the current flow through the spin-orbit  
12 coupled material (iridates here), which makes it a self-consistent method independent of the individual  
13 resistivity values of the two layers. However, in some materials additionally a field-like torque is also  
14 observed, which is parallel to the Oersted field (along the z-axis) and which can be combined into a  
15 single perpendicular torque  $\tau_{\perp}$  which leads to a transverse field  $H_T$ [42,43]. In this case the ratio between  
16 the two torques can no longer be used to determine spin-orbit effects. This field-like torque has been  
17 shown to be highly dependent on the spin-orbit coupled layer thickness, the ferromagnet thickness, the  
18 saturation magnetization and the relative strengths of spin Hall and Rashba effects[42,44–46], changing  
19 in magnitude and sign dependent on all these parameters.

20 The first technique used was spin-torque ferromagnetic resonance (ST-FMR) to determine the spin Hall  
21 angle in  $Sr_2IrO_4$  as shown in Fig 2b. This technique passes an rf-current through a bilayer of the  
22 iridate/permalloy and the output mixing-voltage is determined as a function of the resonance  
23 frequency. This mixing voltage is analytically fitted to symmetric ( $S$ ) and antisymmetric ( $A$ ) components  
24 which can be converted into a spin Hall angle[47]; this has been found to be 0.06 for 5 nm of  $Sr_2IrO_4$  and  
25 0.11 for 10 nm of  $Sr_2IrO_4$  (Fig 2c). The second technique is based on second-harmonic Hall  
26 measurements (SHH), which measures the transverse second harmonic voltage signal arising from a low-  
27 frequency ac-current through a Hall bar. As a reference, Fig 2d gives the first harmonic signal  $R_{1\omega}$  which  
28 is the planar Hall effect. Fig 2e gives the second harmonic signal  $R_{2\omega}$  which has a large  $\cos(\beta)$  signal  
29 (where  $\beta$  is the angle between the applied current and the external field  $H_{ext}$ ), which is related to  $H_{OOP}$   
30 and a small  $\cos(3\beta)$  signal, which is related to  $H_T$ . The spin Hall angle for each direction can be calculated  
31 individually from each of the components[47] by providing the resistivity of each of the layers as a

1 model parameter. Although the fitting of this data (Fig 2f,g) gives spin Hall angles of 0.6 for a 5 nm  
2  $\text{Sr}_2\text{IrO}_4$  layer and 0.4 for a 10 nm  $\text{Sr}_2\text{IrO}_4$  layer, we elaborate below why these are likely to be inaccurate.  
3 The field-like torque is small in this material, as concluded from the observed low  $A$  component for the  
4 ST-FMR and a small  $H_T$  value in SHH. The deviation between the measured spin Hall angles from the two  
5 different techniques is large ( $\sim 0.1$  for ST-FMR and  $\sim 0.5$  for SHH). The ST-FMR spin Hall angle for  $\text{Sr}_2\text{IrO}_4$  is  
6 similar to the 0.07 in a reference Pt material (with the same sign), using the same technique and  
7 ferromagnet layer thickness[47]. The ST-FMR should give reliable values due to the low field-like torque  
8 in this material. The SHH method gives a 0.03 spin Hall angle for the reference Pt, comparable to its ST-  
9 FMR value. However, the deviation for the SHH measurement in  $\text{Sr}_2\text{IrO}_4$  is likely due to the large  
10 resistivity mismatch between NiFe ( $20 \mu\Omega \text{ cm}$ ) and  $\text{Sr}_2\text{IrO}_4$  ( $1\,000\,000 \mu\Omega \text{ cm}$ ), which makes this SHH  
11 technique less accurate. Thermal effects can also play a role in this measurement. Nevertheless, the  
12 large spin Hall angle from this shows that the spin Hall angle is at least comparable to Pt, a good spin  
13 Hall material, where the promising nature of  $\text{Sr}_2\text{IrO}_4$  comes from the strong spin-orbit electronic  
14 structure at the Fermi level.

15 In contrast, the sister compound  $\text{SrIrO}_3$  is a metallic system on the border of a metal-insulator transition  
16 for this strain state[31,33]. The symmetric  $S$  component in the ST-FMR signal (Fig. 3a) looks,  
17 qualitatively, similar to the signal observed in  $\text{Sr}_2\text{IrO}_4$  with a similar measured voltage output signal. The  
18 ST-FMR signal (Fig 3a) is not unlike  $\text{Sr}_2\text{IrO}_4$  for the  $S$  component. However, the  $A$  component is much  
19 larger and of an opposite sign than for the  $\text{Sr}_2\text{IrO}_4$ , indicating a large field-like torque of opposite sign to  
20 the Oersted field. The spin Hall angle calculated from this type of ST-FMR measurement in  $\text{SrIrO}_3$  is not  
21 able to account for this field-like torque, so only a reduced spin Hall angle of about 0.1 can be calculated  
22 from this method. SHH measurements determine  $\tau_{DL}$  and  $\tau_L$  and their corresponding spin Hall angles  
23 individually, which makes it more suitable for this material with a sizeable field-like torque. The first  
24 harmonic planar Hall effect  $R_{1\omega}$  (Fig 3c) is similar to  $\text{Sr}_2\text{IrO}_4$  in shape, while the second harmonic signal  
25 has additional strong contributions for  $\text{SrIrO}_3$ . The  $\tau_L$  with its  $\cos(3\beta)$  signal is large in this measurement  
26 as seen in Fig 3d. Thicker  $\text{SrIrO}_3$  films (with identical NiFe ferromagnets) show an increase in  $H_{OOP}$ , and  
27 thus a stronger charge-to-spin conversion (Fig 3e), with a corresponding decrease in  $H_T$  (Fig 3f). The spin  
28 Hall angle from these two techniques is different since the SHH does not include  $\tau_L$  in its calculations.  
29 The spin Hall angle for a 3 nm thin  $\text{SrIrO}_3$  film is around 0.1, which is similar to that observed in  
30 Ta[46,48]. Interestingly, the spin Hall angle increases for thicker samples. Our measurements  
31 demonstrated a value as large as 0.4 on a 13 nm sample, which is comparable to that reported in W[30]

1 and much larger than the small, positive spin Hall angles with small field-like-torque as in Au[28] and  
2 Pt[29].

3 The resistivity of SrIrO<sub>3</sub> decreases for samples with higher thickness, which is opposite to the trend that  
4 the spin Hall angle increases for thicker samples. The popular belief, based on the demonstration in  
5 heavy metals[26], is that when the crystal structure does not change, samples with higher resistivity  
6 exhibit higher spin Hall angles. In addition, the lowering of the sample resistivity with increasing  
7 thickness is accompanied by a lowering of the carrier concentration. A similar trend has previously been  
8 observed in topological insulators[49,50]. As found previously (Fig 1e), a metal-insulator  
9 transition[31,33] occurs when increasing the thickness from 5 to 10 nm, and this is also the thickness  
10 regime where the resistivity and carrier concentration drastically decrease.

11 We relate the observed trends in spin Hall angle  $\theta_{SH}$ , and carrier concentration ( $n_e$ ) using the following  
12 expression

13 
$$\theta_{SH} = \frac{J_s}{J_c} \propto \frac{2\xi p_0 g^{\uparrow\downarrow}}{\pi m_n} \quad (1)$$

14 which was derived from (i) a semiclassical model[51,52] for charge current induced spin potential in  
15 spin-orbit materials that received numerous experimental confirmation on diverse materials, in  
16 conjunction with (ii) a widely used semiclassical model (see the details of the derivation in the  
17 Supplemental Material[47]) for spin current absorption at the ferromagnet-spin-orbit metal  
18 interface[54]. Here  $0 \leq \xi \leq 1$  is the current shunting in the ferromagnet[51],  $0 \leq p_0 \leq 1$  is the degree of  
19 spin-momentum locking (SML) in the spin-orbit material[51,52],  $g^{\uparrow\downarrow}$  is the real part of the interface spin-  
20 mixing conductance in units of  $m^{-2}$  [53], and  $m_n$  is the number of modes per unit cross-section of the  
21 SML channel which can be calculated from the Fermi wavevector  $k_F$ , of the material as  $m_n = \frac{k_F^2}{2\pi}$  [54].  
22 The Fermi wavevector  $k_F$  of the material is related to the measured carrier concentration  $n_e$  using  $k_F =$   
23  $\sqrt[3]{3\pi^2 n_e}$ . Note that the dependence on  $\xi$ ,  $p_0$ , and  $m_n$  in Eq. 1 arises due to argument (i) based on which  
24 we make arguments below. The dependence on  $g^{\uparrow\downarrow}$  in Eq. 1 arises due to argument (ii).

25 Eq. 1 suggests an increasing trend of the spin Hall angle with the decreasing electron density, which is in  
26 agreement with our experimental observations in Figs. 3(f) and 4(a), respectively. We have compared  
27 the measured spin Hall angle data with  $x/k_F^2$  in Fig. 4(b), where  $x$  is a fitting parameter and  $k_F$  is  
28 estimated from the measured electron density. The  $1/k_F^2$  dependence in Eq. 1 suggests a saturation in  
29 spin Hall angles for thicker samples since the measured electron density saturates above 10 nm. Such

1 saturation is in agreement with similar report[54] of spin Hall angle in SrIrO<sub>3</sub> grown on SrTiO<sub>3</sub> substrates.  
2 Using measured values of  $g^{\uparrow\downarrow}$  [47] and an estimated  $\xi \approx 0.1$  (rough estimation based on resistivity  
3 ratios), we roughly estimate the degree of spin-momentum locking  $p_0$  in Sr<sub>2</sub>IrO<sub>4</sub> as 0.07 and in SrIrO<sub>3</sub> as  
4 0.2-0.6. The estimated large value of  $p_0$  in SrIrO<sub>3</sub> is comparable to that typically seen for topological  
5 insulators[55–61], however, careful spin-potentiometric measurements need to be done for  
6 confirmation of the estimated  $p_0$  which we leave as future work.

7 The observation that both resistivity and electron density are decreasing for thicker samples imply a  
8 larger electron mean free path  $\lambda$ , for thicker samples. We estimate[53] the mean free path using[47]:

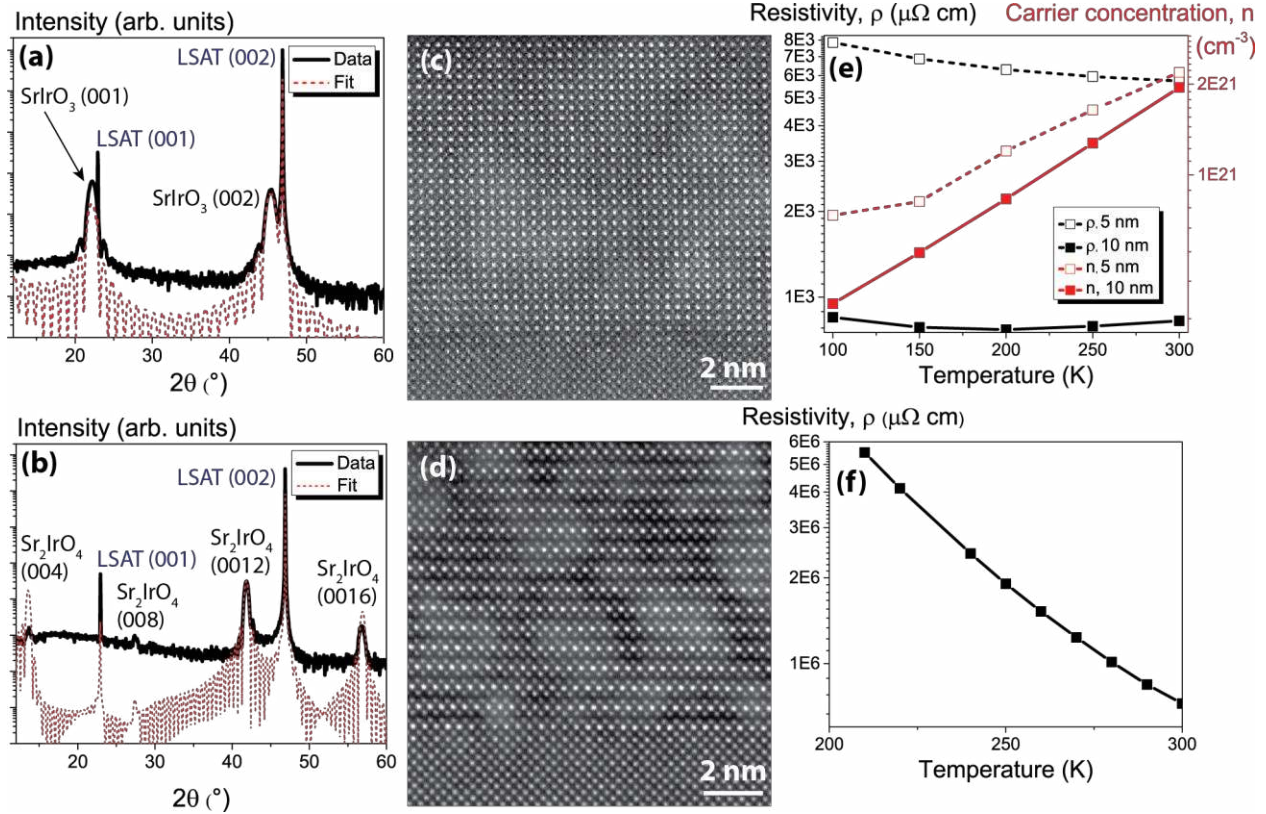
$$9 \quad \lambda = h/(q^2 \rho m_n). \quad (2)$$

10 The estimated mean free path is ~60 pm for 3 nm thick sample which increases and saturates to ~1 nm  
11 for samples thicker than 8 nm, as shown in Fig 4b.

12 So, while in heavy metals it is commonly assumed that an increase in resistivity gives larger spin Hall  
13 angles, the thickness dependent spin Hall angle measurements in SrIrO<sub>3</sub> show that this relationship does  
14 not hold, but rather it is the carrier concentration that determines the efficiency. While in most  
15 materials the carrier concentration and resistivity are anti-correlated, here this correlation is broken, like  
16 in topological insulators. As already shown by previous work, the Weyl semimetal nature of SrIrO<sub>3</sub>  
17 suggests the existence of band-crossing effects. Such a topological nature further manifests itself in the  
18 large degree of spin-momentum locking  $p_0$  of 0.2-0.6, due to the Dirac cone like nature at the Fermi  
19 surface in SrIrO<sub>3</sub>, producing a large spin Hall angle of 0.3-0.5 and a large degree of field-like torque. In  
20 contrast, as expected from prior studies, Sr<sub>2</sub>IrO<sub>4</sub>, which does not have a topological nature to its  
21 electronic structure exhibits a reduced spin Hall angle of ~0.1 (comparable to Pt) and small field-like-  
22 torque while still being promising with its spin-orbit dominated electronic structure. Finally, the large  
23 tunability of electronic structure through crystal chemistry and epitaxial constraint in these oxides make  
24 it possible to further explore relationships and patterns in the search of larger spin Hall angles for  
25 efficient charge and spin interconversion for low power spin logic devices.



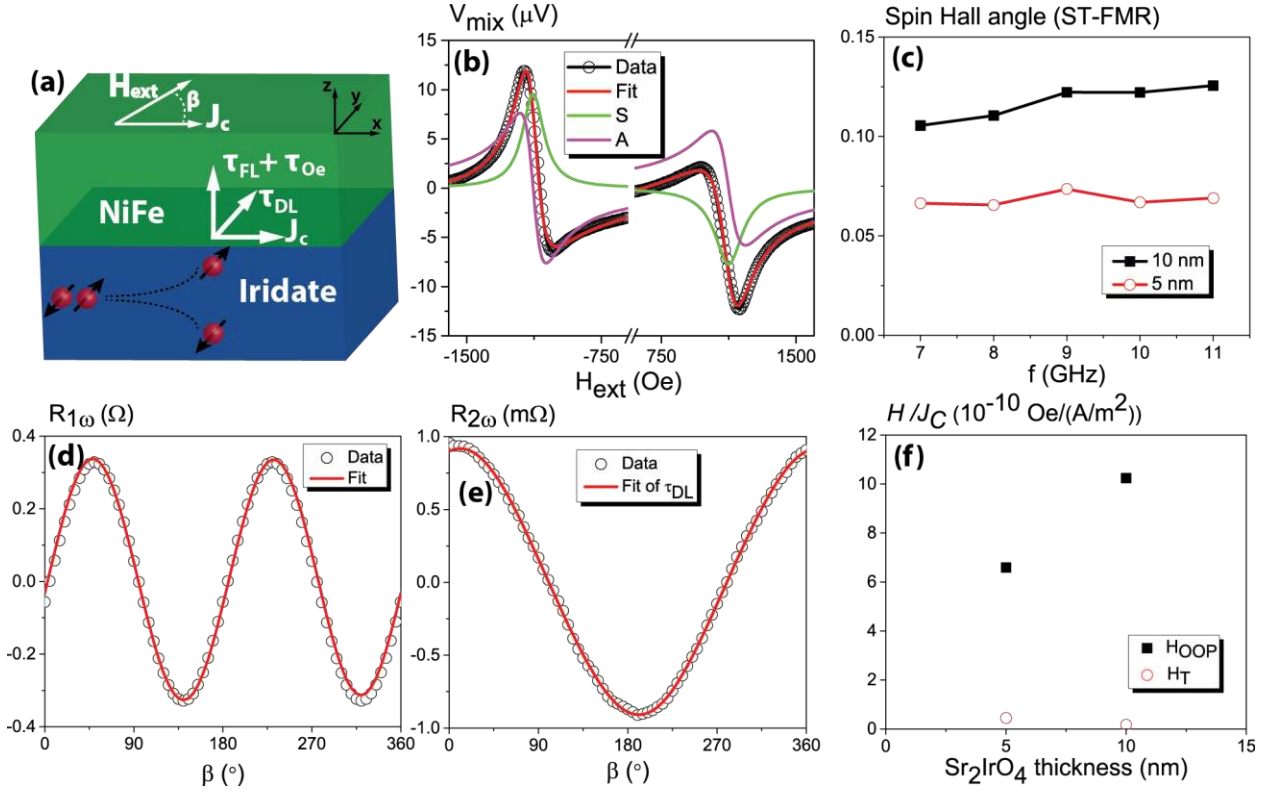
# 1 Figures



2

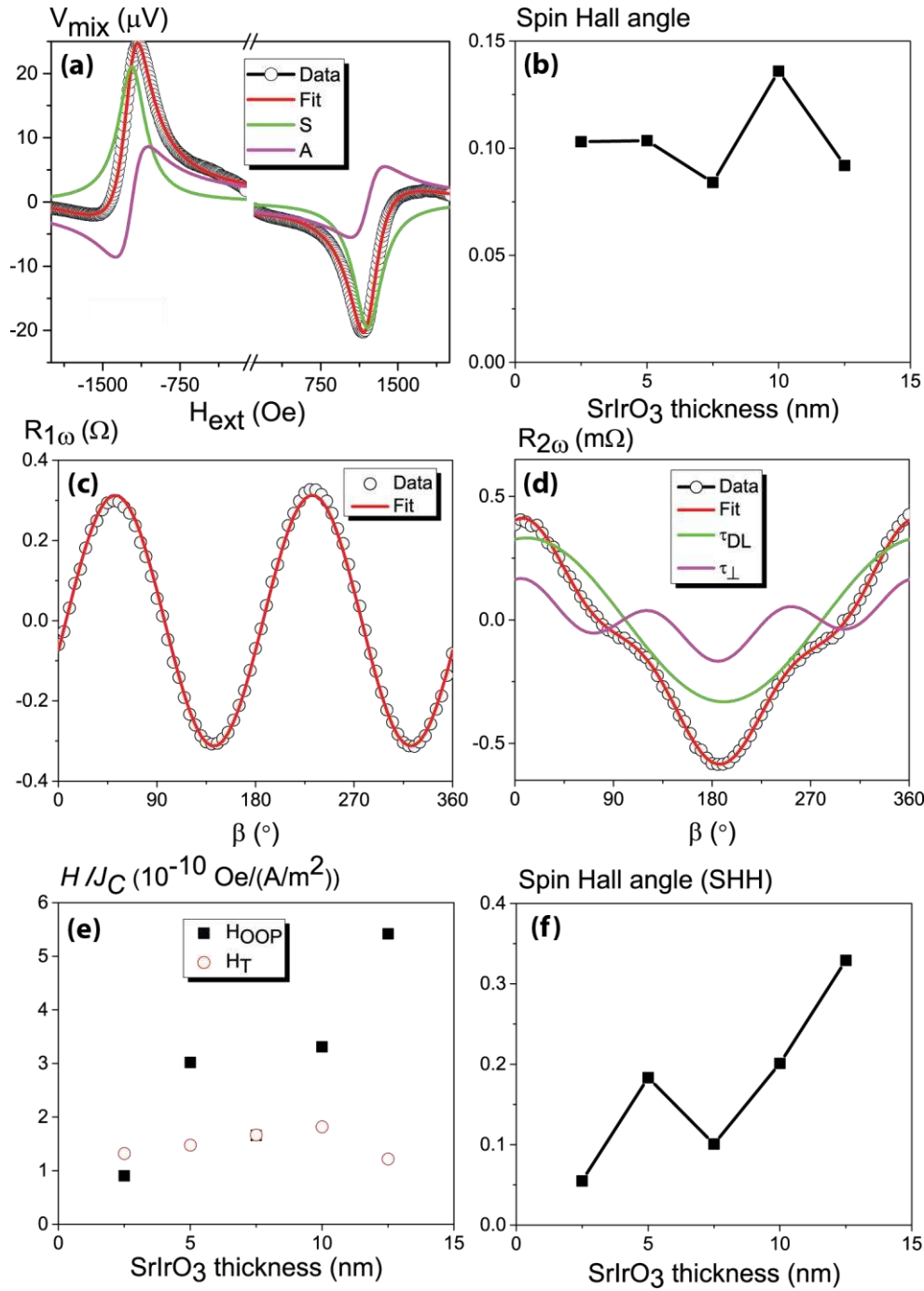
3 FIG. 1. (a,b) X-Ray Diffraction scan of SrIrO<sub>3</sub> and Sr<sub>2</sub>IrO<sub>4</sub>, along with a diffraction pattern calculated from  
 4 their simulated crystal structures. The agreement between the theoretical fits and the data shows that  
 5 the right crystal structures have been formed. Lattice parameters are determined from the Bragg peak  
 6 (00l) indices to be LSAT (substrate) = 3.87 Å, SrIrO<sub>3</sub> = 3.98 Å, and Sr<sub>2</sub>IrO<sub>4</sub> = 25.8 Å. (c,d) Transmission  
 7 Electron Microscopy images of SrIrO<sub>3</sub> and Sr<sub>2</sub>IrO<sub>4</sub>, showing the perovskite and layered structures,  
 8 respectively, of the two materials. A NiFe/AlO<sub>x</sub> top layer is grown on the SrIrO<sub>3</sub>. (e) Resistivity ρ, and  
 9 electron carrier concentration n, mobility of 5 and 10 nm thick films of SrIrO<sub>3</sub>. (f) Resistivity ρ, data for  
 10 10 nm of Sr<sub>2</sub>IrO<sub>4</sub>.

1



2

3 FIG. 2. (a) The different types of torques present in a ferromagnet/iridate bilayer of materials. A charge  
 4 current  $J_c$ , driven through the bilayer, couples to the magnetization  $M$  in the ferromagnet in three ways.  
 5 The anti-damping-like torque  $\tau_{DL}$  acts parallel to the surface and couples to out-of-plane magnetization.  
 6 The field-like torque  $\tau_{FL}$  acts perpendicular to the surface and couples to transverse magnetization, while  
 7 the Oersted torque  $\tau_{Oe}$  acts along the same axis as the field-like torque (combined in  $\tau_L$ ). The external  
 8 magnetic field ( $H_{ext}$ ) can be applied under an in-plane angle  $\beta$  with respect to the current direction. (b)  
 9 ST-FMR resonance line shape for  $\text{Sr}_2\text{IrO}_4$  (10 nm)/NiFe (6 nm) bilayer structure under 5 mA and a  
 10 frequency of 9 GHz oscillating rf current. Lorentzian trial functions extracted symmetric and  
 11 antisymmetric components from the mixing voltage  $V_{mix}$  (the obtained quantity from the measurement),  
 12 represented by the black and green solid lines, respectively. (c) Spin Hall angles extracted from the ST-  
 13 FMR method for different frequencies  $f$ , in 5 and 10 nm of  $\text{Sr}_2\text{IrO}_4$ . (d) First harmonic  $R_{1\omega}$  and (e) Second  
 14 Harmonic  $R_{2\omega}$  signals of the SHH measurement in a  $\text{Sr}_2\text{IrO}_4$  (10 nm)/NiFe (6 nm) bilayer structure under a  
 15 driving field of 10 mA at 5000 Oe.  $R_{1\omega}$  gives the planar Hall effect, while  $R_{2\omega}$  gives a combination of  
 16 different angular contributions, which can be separated into the different contributions. Here only a  
 17  $\cos(\beta)$  contribution is measured, which gives a  $\tau_{DL}$ . (f)  $H_{OOP}$  and (g)  $H_T$  fields as a function of applied  
 18 current, from which the spin Hall angle is calculated.



1

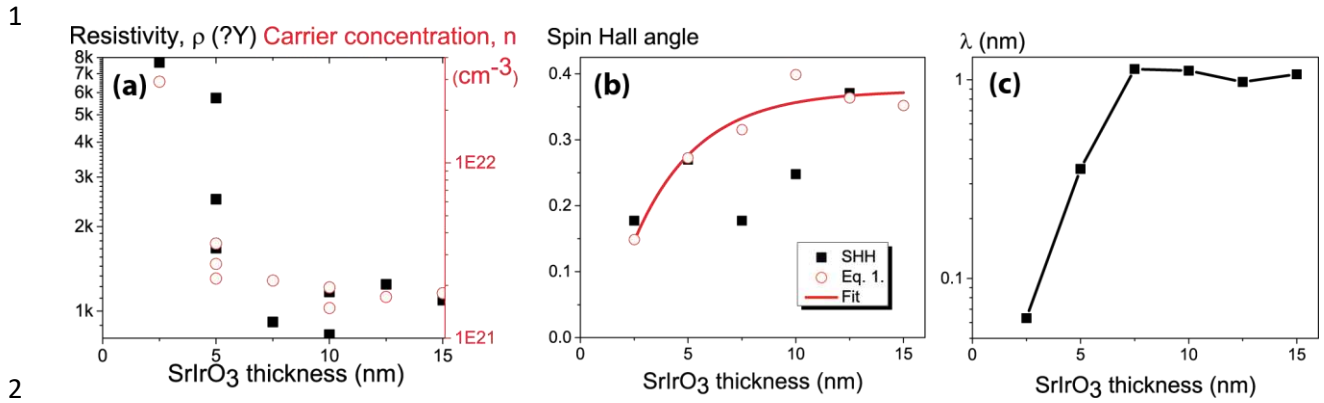
2 FIG. 3. (a) ST-FMR in SrIrO<sub>3</sub> (5 nm)/NiFe (6 nm) under an rf current of 10 mA and a frequency of 9 GHz.

3 (b) Spin Hall angle calculated from ST-FMR. (c)  $R_{1\omega}$  and (d)  $R_{2\omega}$  signals of the SHH measurement in a

4 Sr<sub>2</sub>IrO<sub>4</sub> (10 nm)/NiFe (6 nm) bilayer structure under a driving field of 10 mA at 5000 Oe magnetic field,

5 separated into their components  $\tau_{DL}$  by  $\cos(\beta)$  and  $\tau_{\perp}$  by  $\cos(3\beta)$ . (e)  $H_{OOP}$  and (f)  $H_T$  fields as a function of

6 applied current. (g) Spin Hall angle calculated from SHH measurement from the  $H_{OOP}$ .



1  
2  
3 FIG. 4. (a) Resistivity and carrier concentration calculated from Hall measurements of SrIrO<sub>3</sub> films of  
4 different thickness without capping layer. (b) Calculated spin Hall angles with a fixed fitted  $x$  factor of 5  
5 ( $10^{18} \text{ m}^{-2}$ ) from Eq. 1 with an exponential fit, given together with the measured spin Hall angles. (c)  
6 Electron mean free path  $\lambda$  as determined from Eq. 2 with the same fixed  $x$  factor as in (b).

1 **Acknowledgements**

2 A.S.E., Y.T. and R.R. acknowledge support from the U.S. Department of Energy, Office of Science, Basic  
3 Energy Sciences, Materials Sciences and Engineering Division under Contract No. DE-AC02-05-CH11231  
4 within the Quantum Materials program (KC2202). Portions of the devices were fabricated in the UC  
5 Berkeley Marvell Nanofabrication Laboratory. M.DC., X.H., J.-P.W. and R.R. were supported in part by  
6 ASCENT, one of six centers in JUMP, a Semiconductor Research Corporation (SRC) program sponsored by  
7 DARPA. Portions of this work were conducted in the Minnesota Nano Center, which is supported by the  
8 National Science Foundation through the National Nano Coordinated Infrastructure Network (NNCI)  
9 under Award Number ECCS-1542202.

## 1 References

- 2 [1] E. Dagotto. Nanoscale Phase Separation and Colossal Magnetoresistance. (Springer-Verlag Berlin  
3 Heidelberg, 2003).
- 4 [2] N. A. Spaldin and R. Ramesh. Progress in multiferroics and magnetoelectrics (unpublished). Nat.  
5 Mater. (2019).
- 6 [3] S. Catalano, M. Gibert, J. Fowlie, J. Íñiguez, J.-M. Triscone, and J. Kreisel. Rare-earth nickelates  
7 RNiO<sub>3</sub>: thin films and heterostructures. Reports Prog. Phys. **81**, 046501 (2018).
- 8 [4] J. Wang, J. B. Neaton, H. Zheng, V. Nagarajan, S. B. Ogale, B. Liu, D. Viehland, V. Vaithyanathan, D.  
9 G. Schlom, U. V. Waghmare, *et al.* Epitaxial BiFeO<sub>3</sub> multiferroic thin film heterostructures. Science  
10 **299**, 1719–1722 (2003).
- 11 [5] N. Vlietstra, J. Shan, V. Castel, B. J. Van Wees, and J. Ben Youssef. Spin-Hall magnetoresistance in  
12 platinum on yttrium iron garnet: Dependence on platinum thickness and in-plane/out-of-plane  
13 magnetization. Phys. Rev. B **87**, 184421 (2013).
- 14 [6] W. Witczak-Krempa, G. Chen, Y. B. Kim, and L. Balents. Correlated Quantum Phenomena in the  
15 Strong Spin-Orbit Regime. Annu. Rev. Condens. Matter Phys. **5**, 57–82 (2014).
- 16 [7] Z. Cheng, X. Wang, S. Dou, H. Kimura, and K. Ozawa. Improved ferroelectric properties in  
17 multiferroic BiFeO<sub>3</sub> thin films through La and Nb codoping. Phys. Rev. B **77**, 092101 (2008).
- 18 [8] S. Majumdar and S. Van Dijken. Pulsed laser deposition of La<sub>1-x</sub>Sr<sub>x</sub>MnO<sub>3</sub>: Thin-film properties and  
19 spintronic applications. J. Phys. D. Appl. Phys. **47**, 034010 (2014).
- 20 [9] E. Lesne, Y. Fu, S. Oyarzun, J. C. Rojas-Sánchez, D. C. Vaz, H. Naganuma, G. Sicoli, J.-P. Attané, M.  
21 Jamet, E. Jacquet, *et al.* Highly efficient and tunable spin-to-charge conversion through Rashba  
22 coupling at oxide interfaces. Nat. Mater. **15**, 1261–1266 (2016).
- 23 [10] J. H. Haeni, P. Irvin, W. Chang, R. Uecker, P. Reiche, Y. L. Li, S. Choudhury, W. Tian, M. E. Hawley,  
24 B. Craigo, *et al.* Room-temperature ferroelectricity in strained SrTiO<sub>3</sub>. Nature **430**, 758–761  
25 (2004).
- 26 [11] N. Sato, F. Xue, R. M. White, C. Bi, and S. X. Wang. Two-terminal spin-orbit torque  
27 magnetoresistive random access memory. Nat. Electron. **1**, 508–511 (2018).

- 1 [12] M. Cubukcu, O. Boulle, M. Drouard, K. Garello, C. Onur Avci, I. M. Miron, J. Langer, B. Ocker, P.  
2 Gambardella, and G. Gaudin. Spin-orbit torque magnetization switching of a three-terminal  
3 perpendicular magnetic tunnel junction. *Appl. Phys. Lett.* **104**, 042406 (2014).
- 4 [13] M. G. Mankalale, Z. Zhao, J.-P. Wang, and S. S. Sapatnekar. SkyLogic – A proposal for a skyrmion  
5 logic device. arXiv 1811.02016
- 6 [14] S. Manipatruni, D. E. Nikonov, C.-C. Lin, T. A. Gosavi, H. Liu, B. Prasad, Y.-L. Huang, E. Bonturim, R.  
7 Ramesh, and I. A. Young. Scalable energy-efficient magnetoelectric spin–orbit logic. *Nature* **565**,  
8 35–42 (2018).
- 9 [15] S. Manipatruni, D. E. Nikonov, and I. A. Young. Beyond CMOS computing with spin and  
10 polarization. *Nat. Phys.* **14**, 338–343 (2018).
- 11 [16] M. G. Mankalale, Z. Liang, Z. Zhao, C. H. Kim, J.-P. Wang, and S. S. Sapatnekar. CoMET :  
12 Composite-Input Magnetoelectric-. *IEEE J. Explor. Solid-State Comput. Devices Circuits* **3**, 27–36  
13 (2017).
- 14 [17] S. O. Valenzuela and M. Tinkham. Direct electronic measurement of the spin Hall effect. *Nature*  
15 **442**, 176–179 (2006).
- 16 [18] L. Liu, C.-F. Pai, Y. Li, H. W. Tseng, D. C. Ralph, and R. A. Buhrman. Spin-Torque Switching with the  
17 Giant Spin Hall Effect of Tantalum. *Science* **336**, 555–558 (2012).
- 18 [19] Y. K. Kato, R. C. Myers, A. C. Gossard, and D. D. Awschalom. Observation of the Spin Hall. *Science*  
19 **306**, 1910–1913 (2004).
- 20 [20] K. Ando and E. Saitoh. Observation of the inverse spin Hall effect in silicon. *Nat. Commun.* **2**, 626–  
21 629 (2012).
- 22 [21] M. DC, R. Grassi, J. Y. Chen, M. Jamali, D. Reifsnnyder Hickey, D. Zhang, Z. Zhao, H. Li, P.  
23 Quarterman, Y. Lv, *et al.* Room-temperature high spin–orbit torque due to quantum confinement  
24 in sputtered  $\text{Bi}_x\text{Se}_{(1-x)}$  films. *Nat. Mater.* **17**, 800–807 (2018).
- 25 [22] J. C. R. Sánchez, L. Vila, G. Desfonds, S. Gambarelli, J. P. Attané, J. M. De Teresa, C. Magén, and A.  
26 Fert. Spin-to-charge conversion using Rashba coupling at the interface between non-magnetic  
27 materials. *Nat. Commun.* **4**, 2944 (2013).
- 28 [23] A. R. Mellnik, J. S. Lee, A. Richardella, J. L. Grab, P. J. Mintun, M. H. Fischer, A. Vaezi, A. Manchon,

- 1 E.-A. Kim, N. Samarth, *et al.* Spin-transfer torque generated by a topological insulator. *Nature*  
2 **511**, 449–451 (2014).
- 3 [24] Y. Wang, P. Deorani, K. Banerjee, N. Koirala, M. Brahlek, S. Oh, and H. Yang. Topological surface  
4 states originated spin-orbit torques in Bi<sub>2</sub>Se<sub>3</sub>. *Phys. Rev. Lett.* **114**, 257202 (2015).
- 5 [25] M. Jamali, J. S. Lee, J. S. Jeong, F. Mahfouzi, Y. Lv, Z. Zhao, B. K. Nikolic, K. A. Mkhoyan, N.  
6 Samarth, and J.-P. Wang. Giant Spin Pumping and Inverse Spin Hall Effect in the Presence of  
7 Surface and Bulk Spin-Orbit Coupling of Topological Insulator Bi<sub>2</sub>Se<sub>3</sub>. *Nano Lett.* **15**, 7126–7132  
8 (2015).
- 9 [26] E. Sagasta, Y. Omori, S. Vélez, R. Llopis, C. Tollan, A. Chuvilin, L. E. Hueso, M. Gradhand, Y.C.  
10 Otani, and F. Casanova. Unveiling the mechanisms of the spin Hall effect in Ta. *Phys. Rev. B* **98**,  
11 060410(R) (2018).
- 12 [27] T. Tanaka, H. Kontani, M. Naito, T. Naito, D. S. Hirashima, K. Yamada, and J. Inoue. Intrinsic spin  
13 Hall effect and orbital Hall effect in 4d and 5d transition metals. *Phys. Rev. B* **77**, 165117 (2008).
- 14 [28] O. Mosendz, V. Vlaminck, J. E. Pearson, F. Y. Fradin, G. E. W. Bauer, S. D. Bader, and A. Hoffmann.  
15 Detection and quantification of inverse spin Hall effect from spin pumping in permalloy/normal  
16 metal bilayers. *Phys. Rev. B* **82**, 214403 (2010).
- 17 [29] T. Kimura, Y. Otani, T. Sato, S. Takahashi, and S. Maekawa. Room-temperature reversible spin hall  
18 effect. *Phys. Rev. Lett.* **98**, 156601 (2007).
- 19 [30] C. F. Pai, L. Liu, Y. Li, H. W. Tseng, D. C. Ralph, and R. A. Buhrman. Spin transfer torque devices  
20 utilizing the giant spin Hall effect of tungsten. *Appl. Phys. Lett.* **101**, 122404 (2012).
- 21 [31] L. Zhang, Q. Liang, Y. Xiong, B. Zhang, L. Gao, H. Li, Y. B. Chen, J. Zhou, S.-T. Zhang, Z.-B. Gu, *et al.*  
22 Tunable semimetallic state in compressive-strained SrIrO<sub>3</sub> films revealed by transport behavior.  
23 *Phys. Rev. B* **91**, 035110 (2015).
- 24 [32] A. Biswas, K. S. Kim, and Y. H. Jeong. Metal insulator transitions in perovskite SrIrO<sub>3</sub> thin films. *J.*  
25 *Appl. Phys.* **116**, 213704 (2014).
- 26 [33] L. Hao, D. Meyers, M. P. M. Dean, and J. Liu. Novel spin-orbit coupling driven emergent states in  
27 iridate-based heterostructures. *J. Phys. Chem. Solids* 1–15 (2017).
- 28 [34] B. J. Kim, H. Jin, S. J. Moon, J.-Y. Kim, B.-G. Park, C. S. Leem, J. Yu, T. W. Noh, C. Kim, S.-J. Oh, *et al.*



- 1 Novel Jeff = 1/2 Mott State Induced by Relativistic Spin-Orbit Coupling in Sr<sub>2</sub>IrO<sub>4</sub>. Phys. Rev. Lett.  
2 **101**, 076402 (2008).
- 3 [35] Y. F. Nie, P. D. C. King, C. H. Kim, M. Uchida, H. I. Wei, B. D. Faeth, J. P. Ruf, J. P. C. Ruff, L. Xie, X.  
4 Pan, *et al.* Interplay of Spin-Orbit Interactions, Dimensionality, and Octahedral Rotations in  
5 Semimetallic SrIrO<sub>3</sub>. Phys. Rev. Lett. **114**, 016401 (2015).
- 6 [36] J. M. Carter, V. V. Shankar, M. A. Zeb, and H. Y. Kee. Semimetal and topological insulator in  
7 perovskite iridates. Phys. Rev. B **85**, 115105 (2012).
- 8 [37] Z. T. Liu, M. Y. Li, Q. F. Li, J. S. Liu, W. Li, H. F. Yang, Q. Yao, C. C. Fan, X. G. Wan, Z. Wang, *et al.*  
9 Direct observation of the Dirac nodes lifting in semimetallic perovskite SrIrO<sub>3</sub> thin films. Sci. Rep.  
10 **6**, 30309 (2016).
- 11 [38] A. S. Patri, K. Hwang, H. Lee, and Y. B. Kim. Theory of Large Intrinsic Spin Hall Effect in Iridate  
12 Semimetals. Sci. Rep. **8**, 8052 (2018).
- 13 [39] J. H. Gruenewald, J. Nichols, J. Terzic, G. Cao, J. W. Brill, and S. S. A. Seo. Compressive strain-  
14 induced metal-insulator transition in orthorhombic SrIrO<sub>3</sub> thin films. J. Mater. Res. **29**, 2491–2496  
15 (2014).
- 16 [40] C. Rayan Serrao, J. Liu, J. T. Heron, G. Singh-Bhalla, A. Yadav, S. J. Suresha, R. J. Paull, D. Yi, J.-H.  
17 Chu, M. Trassin, *et al.* Epitaxy-distorted spin-orbit Mott insulator in Sr<sub>2</sub>IrO<sub>4</sub> thin films. Phys. Rev. B  
18 **87**, 085121 (2013).
- 19 [41] J. Nichols, J. Terzic, E. G. Bittle, O. B. Korneta, L. E. De Long, J. W. Brill, G. Cao, and S. S. A. Seo.  
20 Tuning electronic structure via epitaxial strain in Sr<sub>2</sub>IrO<sub>4</sub> thin films. Appl. Phys. Lett. **102**, 141908  
21 (2013).
- 22 [42] Y. Ou, C. F. Pai, S. Shi, D. C. Ralph, and R. A. Buhrman. Origin of fieldlike spin-orbit torques in  
23 heavy metal/ferromagnet/oxide thin film heterostructures. Phys. Rev. B **94**, 140414(R) (2016).
- 24 [43] T. D. Skinner, M. Wang, A. T. Hindmarch, A. W. Rushforth, A. C. Irvine, D. Heiss, H. Kurebayashi,  
25 and A. J. Ferguson. Spin-orbit torque opposing the Oersted torque in ultrathin Co/Pt bilayers.  
26 Appl. Phys. Lett. **104**, 062401 (2014).
- 27 [44] R. Ramaswamy, X. Qiu, T. Dutta, S. D. Pollard, and H. Yang. Hf thickness dependence of spin-orbit  
28 torques in Hf/CoFeB/MgO heterostructures. Appl. Phys. Lett. **108**, 202406 (2016).

- 1 [45] J. Kim, J. Sinha, M. Hayashi, M. Yamanouchi, S. Fukami, T. Suzuki, S. Mitani, and H. Ohno. Layer  
2 thickness dependence of the current-induced effective field vector in Ta|CoFeB|MgO. *Nat.*  
3 *Mater.* **12**, 240–245 (2013).
- 4 [46] G. Allen, S. Manipatruni, D. E. Nikonov, M. Doczy, and I. A. Young. Experimental demonstration of  
5 the coexistence of spin Hall and Rashba effects in  $\beta$ -tantalum/ferromagnet bilayers. *Phys. Rev. B*  
6 **91**, 144412 (2015).
- 7 [47] See Supplemental Material at [URL will be inserted by publisher] for the details on the  
8 measurement technique and the extraction of the spin Hall angles from the ST-FMR and SHH  
9 techniques and the derivation of the spin Hall angle and mean free path equations.
- 10 [48] L. Liu, T. Moriyama, D. C. Ralph, and R. A. Buhrman. Spin-torque ferromagnetic resonance  
11 induced by the spin Hall effect. *Phys. Rev. Lett.* **106**, 036601 (2011).
- 12 [49] Y. S. Kim, M. Brahlek, N. Bansal, E. Edrey, G. A. Kapilevich, K. Iida, M. Tanimura, Y. Horibe, S.-W.  
13 Cheong, and S. Oh. Thickness-dependent bulk properties and weak antilocalization effect in  
14 topological insulator Bi<sub>2</sub>Se<sub>3</sub>. *Phys. Rev. B* **84**, 073109 (2011).
- 15 [50] J. Suh, K. M. Yu, D. Fu, X. Liu, F. Yang, J. Fan, D. J. Smith, Y.-H. Zhang, J. K. Furdyna, C. Dames, *et al.*  
16 Simultaneous Enhancement of Electrical Conductivity and Thermopower of Bi<sub>2</sub>Te<sub>3</sub> by  
17 Multifunctionality of Native Defects. *Adv. Mater.* **27**, 3681–3686 (2015).
- 18 [51] S. Sayed, S. Hong, and S. Datta. Multi-Terminal Spin Valve on Channels with Spin-Momentum  
19 Locking. *Sci. Rep.* **6**, 35658 (2016).
- 20 [52] S. Sayed, S. Hong, and S. Datta. Transmission Line Model for Materials with Spin-Momentum  
21 Locking. *Phys. Rev. Appl.* **10**, 054044 (2018).
- 22 [53] Y. T. Chen, S. Takahashi, H. Nakayama, M. Althammer, S. T. B. Goennenwein, E. Saitoh, and G. E.  
23 W. Bauer. Theory of spin Hall magnetoresistance (SMR) and related phenomena. *Phys. Rev. B* **87**,  
24 144411 (2013).
- 25 [54] T. Nan, T. J. Anderson, J. Gibbons, K. Hwang, N. Campbell, H. Zhou, Y. Q. Dong, and G. Y. Kim.  
26 Anisotropic spin-orbit torque generation in epitaxial SrIrO<sub>3</sub> by symmetry design. *arXiv*  
27 1808.06650 (2018).
- 28 [55] J. Tang, L.-T. Chang, X. Kou, K. Murata, E. S. Choi, M. Lang, Y. Fan, Y. Jiang, M. Montazeri, W.

- 1 Jiang, *et al.* Electrical Detection of Spin-Polarized Surface States Conduction in  $(\text{Bi}_{0.53}\text{Sb}_{0.47})_2\text{Te}_3$   
2 Topological Insulator. *Nano Lett.* **14**, 5423–5429 (2014).
- 3 [56] L. Liu, A. Richardella, I. Garate, Y. Zhu, N. Samarth, and C. T. Chen. Spin-polarized tunneling study  
4 of spin-momentum locking in topological insulators. *Phys. Rev. B* **91**, 235437 (2015).
- 5 [57] F. Yang, S. Ghatak, A. A. Taskin, K. Segawa, Y. Ando, M. Shiraishi, Y. Kanai, K. Matsumoto, A.  
6 Rosch, and Y. Ando. Switching of charge-current-induced spin polarization in the topological  
7 insulator  $\text{BiSbTeSe}_2$ . *Phys. Rev. B* **94**, 075304 (2016).
- 8 [58] C. H. Li, O. M. J. Van't Erve, J. T. Robinson, Y. Liu, L. Li, and B. T. Jonker. Electrical detection of  
9 charge-current-induced spin polarization due to spin-momentum locking in  $\text{Bi}_2\text{Se}_3$ . *Nat.*  
10 *Nanotechnol.* **9**, 218–224 (2014).
- 11 [59] J. S. Lee, A. Richardella, D. R. Hickey, K. A. Mkhoyan, and N. Samarth. Mapping the chemical  
12 potential dependence of current-induced spin polarization in a topological insulator. *Phys. Rev. B*  
13 **92**, 155312 (2015).
- 14 [60] J. Tian, I. Miotkowski, S. Hong, and Y. P. Chen. Electrical injection and detection of spin-polarized  
15 currents in topological insulator  $\text{Bi}_2\text{Te}_2\text{Se}$ . *Sci. Rep.* **5**, 14293 (2015).
- 16 [61] A. Dankert, J. Geurs, M. V. Kamalakar, S. Charpentier, and S. P. Dash. Room temperature  
17 electrical detection of spin polarized currents in topological insulators. *Nano Lett.* **15**, 7976–7981  
18 (2015).